

Development and application of a street-level meteorology and pollutant tracking system (S-TRACK)

Huan Zhang^{1,2}, Sunling Gong^{1*}, Lei Zhang^{1*}, Jianjun He¹, Yaqiang Wang¹, Lixin Shi^{2,3}, Jingyue Mo¹, Huabing Ke¹, Shuhua Lu¹

5 ¹ State Key Laboratory of Severe Weather & Key Laboratory of Atmospheric Chemistry of CMA, Chinese Academy of Meteorological Sciences, Beijing 100081, China

² Key Laboratory of Meteorology and Ecological Environment of Hebei Province, Shijiazhuang 050000, China

³ Meteorological Institute of Hebei Province, Shijiazhuang 050000, China

Correspondence to: Sunling Gong (gongsl@cma.gov.cn) and Lei Zhang (leiz09@cma.gov.cn)

10 **Abstract.** A multi-model simulation system for street level circulation and pollutant tracking (S-TRACK) has been developed by integrating the Weather Research and Forecasting (WRF), the STAR-CCM+ (Computational Fluid Dynamics model - (CFD)) and the Flexible Particle (FLEXPART) models. The winter wind environmental characteristics and the potential impact of a traffic sources on nearby receptor sites
15 (about 300 to 400 m) in a city district of Jinshui district of Zhengzhou, China are analyzed with the system for January 2019. It is found that complex building layouts change the structure of the wind field and thus have an impact on the transport of pollutants.~~the existence of buildings complicates the structure of the wind fields.~~ The wind speed inside the building block is smaller than the background wind speed due to
20 the dragging effect of dense buildings. Ventilation is better when the dominant airflow is in the same direction as the building layout. Influenced by the building layout, the local circulations show that the windward side of the building is mostly the divergence zone and the leeward side is mostly the convergence zone, which is more obvious for high buildings and influencing air pollution transport at the street level. With the hypothesis
25 that the traffic sources are uniformly distributed on each road and with identical traffic volumes, the potential contribution ratios of four traffic sources to certain specific sites

under the influence of the street-level circulations are estimated with the method of residence time analysis. It is found that the contribution ratio varies with the height of the receptor site. As a result of the generally upward motion in the airflow, the position with the greatest potential contribution ratio from the four road traffic sources is located on a certain height (about 15m in this study). The potential contribution of a road to one of the receptor sites is also investigated under different wind directions. The established system and the results can be used to understand the characteristics of urban wind environment and to help the air pollution control planning in urban areas.~~Using the traffic source (line source) on a road within a city block, the system was applied to investigate the potential impact of a line source on specific sites under the influence of the street-level circulations. The potential contribution ratio was estimated by the method of residence time analysis and to a particular site found to vary with the height of the site with a peak not at the ground but on a certain height. The results of the study are helpful to understand the characteristics of wind environment and effect of traffic emissions in the area, which is important to improve urban living environment and control air pollution.~~

1. Introduction

In recent decades, with the continuous development of urban construction in China, urban environmental problems have become increasingly serious and attracted widespread attentions. According to the 2019 China Ecological Environment Status Bulletin, 180 of 337 cities at the prefecture level exceeded ambient air quality standards. The complex building layouts and differences in thermal structures within cities lead to extremely complicated meteorological characteristics and pollutant transport in urban

areas (Lei et al., 2012; Fernando et al., 2010; Aynsley, 1989). Though the
50 ~~transport~~diffusion of atmospheric pollution in urban areas is widely studied, the study on
tracking the sources of pollutants on the street-level is still lacking due to limitations in
research methods.

~~The~~Researches on the street-level atmospheric environment ~~is~~are mainly divided
into three methods: field measurements (Macdonald et al., 1997), laboratory simulation
55 research (Mavroidis et al., 2003), and model simulations (Steenburgh et al., 2015;
Hendricks et al., 2007; Yucong et al., 2014). The model simulation has become one of
the main methods for studying environmental problems at the street-level due to the easy
control of simulation conditions and simple processing steps. The Computational Fluid
Dynamics (CFD) is a numerical simulation method to study the fluid thermal-dynamic
60 problems and is now widely used in the studies related to microscale problems within the
urban canopy (Gosman, 1999). The core of CFD simulation method is to solve the
Navier-Stokes equations. Depending on the turbulence closure scheme, CFD pre-
processing models can be divided into three types: Direct numerical simulation (DNS),
Reynolds-averaged Navier–Stokes (RANS) (Liu et al., 2018; Zheng et al., 2015; Milliez
65 and Carissimo, 2008) and Large eddy simulation (LES) (Kurppa et al., 2018; Li et al.,
2008; Sada and Sato, 2002). The choice among the three methods depends on the costs
and objectives. One of the most important issues ~~in~~ using CFD technology in the
~~research~~atmospheric environment problems on the street-level is to obtain accurate
initial and boundary conditions (Ehrhard et al., 2000). To solve this problem, the multi-
70 scale coupling method is revealed as a good solution, which uses the meteorological
information from mesoscale model as the initial and boundary conditions to drive CFD

(Nelson et al., 2016). Tewari et al. (2010) proved that the CFD simulation was improved significantly when the results of Weather Research and Forecasting (WRF) model were used as the initial and boundary conditions. With the WRF model, the community
75 multiscale air quality (CMAQ) model, and the CFD (RANS) approach, Kwak et al. (2015) built an urban air quality modelling system, which ~~shown~~ presented a better performance than the WRF-CMAQ model in simulating NO₂ and O₃ concentrations.

~~Nevertheless, There is still a lack of research on pollutant sources in the study of the~~
street-level air ~~pollution~~ pollutant transport resulted from the nearby sources was still not
80 fully investigated. The Flexible Particle (FLEXPART) model (Stohl et al., 2005; Stohl, 2003) is a gas-block trajectory-particle ~~dispersion~~ diffusion model based on the Lagrangian particle method. The FLEXPART model can track the transport of tracers via forward or backward simulation. Different from Eulerian model, the Lagrangian model is not restricted by the Courant–Friedrichs–Lewy (CFL) condition (Stam, 1999) and thus,
85 the integration process in the Lagrangian model can be maintained with high spatial resolution with acceptable computation efficiency. Initially, the FLEXPART model was driven by global meteorological reanalysis data from ECMWF or NCEP. ~~In 2006,~~ Fast and Easter (2006) developed a FLEXPART version that used the WRF model output and was optimized with technical level and output results.
90 ~~FLEXPART model together and optimized when it came to technical level and output results.~~ Nowadays, the WRF-FLEXPART model has been widely used to research the regional transport of air pollutants (Yu et al., 2020; He et al., 2020; Gao et al., 2020; He et al., 2017a; Brioude et al., 2013; De Foy et al., 2011). ~~The FLEXPART model can track the transport and diffusion of tracers via forward or backward simulation. Different~~

95 ~~from Euler's model, the spatial resolution is not affected by the numerical dispersion in~~
~~the integration process and can be maintained with high accuracy during the simulation.~~
~~Therefore, it is suitable to apply FLEXPART model to trace the source of street level air~~
~~pollution.~~ Cécé et al. (2016) firstly applied the FLEXPART model at a small-scale
resolution to analyze potential sources of NO_x in urban areas, with the WRF-LES
100 model results as the driving field. Though FLEXPART has been extensively applied in
medium and long-range transport cases (Madala et al., 2015; Heo et al., 2015; Sandeepan
et al., 2013; Liu et al., 2013), it has been rarely tested for street-level transport and small-
scale resolution grids.

The objective of the present work is to investigate the flow field characteristics and
105 potential impact of traffic sources to receptor sites, under real building scenarios and
meteorological conditions. ~~In this study~~To this end, a multi-model simulation system for
street level circulation and pollutant tracking (S-TRACK) was developed by integrating
the WRF mesoscale, the ~~CFD-STAR-CCM+~~ street scale and the FLEXPART particle
~~dispersion~~diffusion models, and applied to the Jinshui District of Zhengzhou city, Henan
110 Province. Zhengzhou is located in the central of China with four distinct seasons.
According to the Oceanic Niño Index (ONI), an El Niño event occurred in January 2019.
The occurrence of El Niño generally favours a warm winter and weak winter winds in
China that is conducive to occurrence of air pollution. Therefore, the period of January
2019 was selected and simulated for this study. This manuscript is organized as follows.
115 Section 2 presents the model details and the observed data for the model validation.
Section 3 provides the details of the model validation results, the wind environment
characteristics and the potential impact of traffic source on receptor sites in the region.

Section 4 provides the conclusions of the study. to study the flow field characteristics and potential impact of traffic pollution to receptor sites, under real building scenarios and atmospheric conditions.

2. Data and Methods

2.1 S-TRACK description

The S-TRACK system consists of three major components (Fig. 1). The WRF model is used to obtain the mesoscale three dimensions (3D) meteorological datafields, with the initial and boundary conditions provided by NCEP FNL reanalysis data. The CFD model STAR-CCM+, driven by the meteorological data from WRF, is used to obtain compute the refined 3D street-level wind field meteorological data fields with a resolution of 1 m to 100 m in the simulation area, with the initial and boundary meteorological conditions provided by the WRF simulations. With the refined 3D meteorology, tThe FLEXPART model is coupled run to analyze the street-level sources of atmospheric pollution transports of traffic sources at street-level and their potential contribution to specific sites. One should note that some meteorological variables needed by FLEXPART that the STAR-CCM+ cannot provide (Table 1) are obtained from WRF simulations., with driving wind field data from the CFD simulations and other meteorological data from the WRF simulations. The specific coupling scheme of the S-TRACK system is detailed as follows:

I. Run the WRF model (refer to Section 2.2 for specific settings) to obtain meteorological data with a spatial resolution of 1 km × 1 km, including temperature, pressure, humidity, wind, etc.

140 II. Extract the value of temperature (T) and wind (U, V and W) from the WRF
simulation, as the initial and boundary conditions of the STAR-CCM+ simulation. Run
the STAR-CCM+ (refer to Section 2.3 for specific settings) to obtain values of
meteorological variables with a spatial resolution of 1 m - 100 m, including wind field,
surface pressure, and surface sensible heat flux, etc. The 3D street-level grid for STAR-
145 CCM+ is detailed in Section 2.3.1.

III. Match the STAR-CCM+ grids to the WRF grids. As the FLEXPART-WRF
(version 3.3.2) was used here, the grid structure of meteorological input data to
FLEXPART should match the grid structure of WRF model. To this end, a regular fine
grid with a horizontal resolution of 10×10 m was constructed base on the pre-processing
150 system of WRF model (WPS). The urban building height data obtained base on drone
aerial photography was taken as part of the terrain height data in the WPS. Once the
refine grid was established, meteorological variables of the STAR-CCM+ and WRF
model were interpolated into the grid by a nearest-neighbour interpolation method.

IV. Run the backward FLEXPART model (refer to Section 2.4 for specific
155 settings) to obtain the 3D spatial location data of released particles, which was used to
analyse the features of pollutant transport at street-level and potential contribution of
traffic source to specific sites.

2.2 WRF model configuration

~~The WRF-ARW model (version 4.1.2) is used to simulate meteorological fields on~~
160 ~~the urban scale, and the results are used as the initial and boundary conditions to drive~~
~~the CFD model.~~ In this study, the WRF model is configured with four nested domains

(Fig. 2a), with the resolution of $27\text{ km} \times 27\text{ km}$ (85×85 grids), $9\text{ km} \times 9\text{ km}$ (82×82 grids), $3\text{ km} \times 3\text{ km}$ (82×82 grids), and $1\text{ km} \times 1\text{ km}$ (61×61 grids), respectively. Vertically, there are 45 full eta levels from the surface to 100 hPa with 11 levels below 2 km, on which the meteorological fields are used to drive the ~~CFD model~~ STAR-CCM+. The innermost nested region is shown in Fig. 2b, where the area focused in this study is marked with a black box. The initial and boundary conditions of WRF model are obtained from the NCEP re-analysis data (<http://rda.ucar.edu/dataset-s/ds083.2>). The boundary conditions are updated every 6 hr. Table ~~2~~ lists the selected physical parameterization schemes. The time from 12:00 Beijing time (BJT) on December 30, 2018 to 23:00 BJT on January 31, 2019 is chosen as the modelling period, with the simulation results recorded ~~once per~~ every hour.

2.3 ~~CFD~~ STAR-CCM+ configuration

The STAR-CCM+, one of the most commonly used commercial CFD software, was selected for the street-level simulation. Previous studies had found an excellent correlation between STAR-CCM+ simulated and measured values in simulating environmental and meteorological problems at street-level (Santiago et al., 2017; Borge et al., 2018; Jls et al., 2020). The model has ~~powerful~~ functions such as geometric modelling, model pre-processing, the calculation execution, and post-processing of results. ~~It has advantages in meshing and has the ability to analyze fluid flow.~~ More details on STAR-CCM+ can be found at <https://www.plm.automation.siemens.com/global/zh/products/simcenter/STAR-CCM.html>.

2.3.1 3D street-level ~~model construction and grid generation~~ setting

185 The establishment of a 3D geometric model is based on the actual terrain and buildings height data ~~for~~ the simulated area, ~~which is~~ obtained through the drone aerial photography technology. The basic data such as the geometric shape of urban buildings, roof height and vector data of the top of buildings with high resolution, high timeliness and accuracy are used to construct a realistic 3D geometric model for driving the STAR-
190 CCM+ simulation. In the process of model construction, the same shape as the actual building was maintained to reduce the influence of model errors on the calculation results (Fig. 3a). The length, width, and height of the ~~CFD-~~STAR-CCM+ calculation domain are 13 km, 11 km, and 2 km, respectively, among which, nearly 2/3 of the buildings are distributed in the range of 10 - 40 meters, with the average height of the
195 buildings of 32 m. The highest building in the area is 390 m, and the lowest building is 6 m.

The geometric model domain is divided by polyhedral meshes (Figs. 3c). The polyhedral mesh has much fewer cells than the traditional tetrahedral mesh, but ~~it doesn't affect the~~with a similar accuracy of calculation. Under the same number of grid cells, the
200 numerical simulation results of polyhedral grids are more consistent with experimental data than tetrahedral grid cells (Zhang et al., 2020). ~~When splitting the grid, t~~The grid cells on the ground and near the buildings are much denser (Fig. 3b) (the minimum resolution is about 1 m), so that the influence of the building on the flow patterns can be described more finely accurately. In the end, the number of unit grid cells generated is
205 382181, and the number of nodes is 1990224.

2.3.2 Physical model and boundary conditions

The STAR-CCM+ solves the RANS with the realizable k-ε turbulence closure scheme. In order to save computing resources, the RANS turbulence model with realizable k-ε is used in this study (Li et al., 2019; Li et al., 2006; Lei et al., 2004). The governing equations (1-3) of CFD are as follows:

$$\frac{\partial \bar{u}_i}{\partial t} + \bar{u}_j \frac{\partial \bar{u}_i}{\partial x_j} = \frac{1}{\rho} \frac{\partial \bar{p}}{\partial x_i} + \frac{\mu}{\rho} \frac{\partial^2 \bar{u}_i}{\partial x_i \partial x_j} - \frac{\partial}{\partial x_j} (\overline{u'_i u'_j}) + f_i, \quad (1)$$

$$\frac{\partial \bar{u}_i}{\partial x_j} = 0, \quad (2)$$

$$\frac{\partial \bar{T}}{\partial t} + \bar{u}_i \frac{\partial \bar{T}}{\partial x_i} = k \frac{\partial^2 \bar{T}}{\partial x_i^2}, \quad (3)$$

where \bar{u}_x and \bar{u}_y mean the average velocity in west-east and south-north directions, respectively; u'_x and u'_y mean the turbulent variation; ρ means the air density; f_i means the buoyancy; and \bar{T} means the mean temperature.

The ground and building surfaces are set to be no-slip, and the distribution of fluid velocity and pressure near the ground and the building surface is described by the blended wall function. For the coupling of WRF model to STAR-CCM+, the values of temperature and wind from the WRF simulation are extracted to establish the initial and boundary conditions for STAR-CCM+. The initial and boundary conditions (including velocity and temperature) of the calculation domain are obtained from the WRF grid closest to the CFD domain. Since the variables obtained by WRF simulation have a relatively coarse large-resolution of 1 km, the velocity components (U, V and W) and the temperature are interpolated to the boundary of CFD-STAR-CCM+ domain using the

spline interpolation method and the linear interpolation method, respectively. For the turbulence intensity and turbulence viscosity ratio, the lateral and upper boundaries ~~were~~ are set as constants with values of 0.1 and 10, respectively. ~~The simulation time is from 0:00 BJT on 1 January 2019 to 23:00 BJT on 31 January 2019 and the simulation results are saved every 1 hour.~~

2.4 FLEXPART configuration

~~The FLEXPART model is a gas mass trajectory particle diffusion model based on the Lagrange method developed by the Norwegian Atmospheric Research Institute. This study uses wind field data obtained from CFD model in combination with other meteorological data from WRF model to drive the FLEXPART.~~ The simulation area is set to sub-domain B in Figure 3, with a horizontal grid resolution of 10 m × 10 m. The simulation time is from 1:00 BJT 1 January 1, 2019 ~~at 1:00 BJT to 23:00 BJT 30 January 30, 2019 at 23:00 BJT~~. The time step of FLEXPART is 1 s, and the output time interval is 120 s. FLEXPART calculates particle trajectories using analysed winds plus random motions in order to account for turbulence. Simulation results from mesoscale meteorological models (such as WRF) do not resolve individual turbulence cells, although they reproduce the large-scale effects of turbulence. To account for sub-grid turbulence, turbulence options need to turn on in FLEXPART (Stohl and James, 2004). ~~For the backward trajectory simulation~~ However in this study, the turbulence options and ~~the CBL turbulence parameterization scheme~~ are turned off, since the turbulence is already resolved during by the CFD STAR-CCM+ simulation. Through backward trajectory simulation, the impact of traffic source on the receptor sites in the region can

be effectively analyzed. Due to the high number of grids in the region and the fact that increasing the number of released particles leads to consuming more computational resources, the particle residence time is set as 2 h, and 5 tracer particles are released per hour, and the total number of particles released was 3590 tracer particles~~2 tracer particles are released per hour at receptor sites~~ in the course of simulation.

2.5 Meteorological observation data

Hourly near-surface meteorological observations from the Bank School City monitoring site (hereinafter referred as the BSC monitoring site), including 2 m temperature (T), 2 m relative humidity (RH), surface pressure (P), 10 m wind direction (WD) and 10 m wind speed (WS) in January 2019 are used to evaluate the WRF and ~~CFD-STAR-CCM+ model simulation~~ results, with the statistical indexes including Pearson's correlation coefficient (R), root mean square error (RMSE), mean ~~deviation~~ bias (MB) and mean error (ME). The location of the BSC monitoring site (34.802375N, 113.675237E) is shown in Figure 3.

3. Results and discussions

3.1 Model evaluation

The performance of WRF model to simulate meteorological elements is an important basis for ~~CFD-STAR-CCM+~~ and FLEXPART simulations. The hourly meteorological data for January 2019 obtained from the innermost nested simulation of the WRF model is selected to compare with observation data to verify the WRF model. Table 32 lists the statistical results of T, RH, P, and WS. The T and RH are slightly

~~overestimated~~underestimated, with the MB values as 1.86 k and 5.95%, respectively, and
270 the P and WS are ~~underestimated~~overestimated by the WRF model, with the MB values
as 3.66 hpa and 1.44 m s⁻¹, respectively. The R values for T, RH and P are 0.80, 0.70 and
0.98, respectively, ~~passed~~passing the 99% significance test, and indicating that the
variation characteristics of T, RH and P are well reproduced by the WRF model. WS is
generally overestimated by WRF model (Temimi et al., 2020; He et al., 2014), which is
275 also found in the present study with the RMSE of 1.97 m s⁻¹. The performance of the
near-surface meteorology obtained by the WRF simulation is equivalent to previous
studies (He et al., 2017b; Carvalho et al., 2012). ~~In general, the temporal and spatial
variability characteristics of the meteorological field in the area can be well simulated by
the WRF model.~~

280 Since the time-varying boundary conditions in the calculation domain of ~~CFD~~
~~model~~STAR-CCM+ are obtained from WRF model, the simulation performance of WRF
model has an important influence on the ~~CFD~~STAR-CCM+ simulation results. The
wind has an important influence on the transport ~~and diffusion~~ of air pollutants in the
area (Zhang et al., 2015). Figure 4 shows the hourly wind observations and simulations
285 at the BSC monitoring site in January 2019. Both WRF and ~~CFD~~STAR-CCM+
overestimate the wind speed to certain degrees (Fig. 4a). The average of observed wind
speed is 0.92 m s⁻¹, with the value simulated by WRF and by ~~CFD~~STAR-CCM+ is 2.37
m s⁻¹ and 2.00 m s⁻¹, respectively. The R values of WRF and ~~CFD~~STAR-CCM+ are 0.45
and 0.67, respectively, ~~and passed~~passing the 99% significance test, and demonstrating
290 the refined ~~CFD~~STAR-CCM+ wind simulations ~~is~~are superior to that of the WRF. This
might be due to the fact that the resolution of WRF simulation is not fine enough and the

underlying surface is processed in a parameterized way that can't accurately describe the urban surface roughness. For the ~~CFD-STAR-CCM+ model~~, the geometric model is used for the underlying surface, which could better reflect the urban surface conditions compared to parametric methods, ~~but some urban layout settings (such as greenery) are missing in the construction of the geometric model~~. Figure 4b shows the comparison results of the observed and ~~CFD~~-simulated wind directions. It can be seen that the change of the wind direction is captured by ~~CFD model~~the STAR-CCM+ well. The wind direction is verified by hit rates (HR) (Schlünzen and Sokhi, 2008). With desired accuracy between $\pm 45^\circ$, the HR are calculated at 63 and 51 % for STAR-CCM+ and WRF, respectively, indicating that variations in wind direction have been basically captured with a better performance for STAR-CCM+ simulations.

~~In general, WRF-CFD model simulation has good performance. After interpolation processing, they can provide more accurate and refined meteorological fields for FLEXPART model.~~

3.2 The characteristics of the street-level wind fields

In urban areas, the complex spatial structure and layout of buildings have a great influence on the street-level wind field (Liu et al., 2018; Park et al., 2015), which is a crucial meteorological factor that controls the transport ~~and diffusion~~ of air pollutants. The street-level wind field characteristics were simulated by the S-TRACK and discussed comprehensively in this paper for the overall average in January as well as for different background wind directions, i.e., north, south, west and east, respectively.

3.2.1 The average wind field characteristics

Figures 5a-b illustrate the distribution of the average wind streamlines in January at the height of 5 m and 40 m, respectively. At the height of 5 m, the wind field structure is more complicated (Fig. 5a) than that at 40 m (Fig. 5b). The wind speed is relatively ~~larger~~ more intense in the areas where the buildings are sparse and smaller. In addition, the flow fields diverge or converge due to the layout of buildings and streets, causing the wind direction inside blocks differ from the background wind direction greatly. As the density of buildings gradually decreases with the increases of height, this phenomenon diminishes, reflected by the relatively more consistent wind fields at 40 m (Fig. 5b). ~~At the height of 40 m (Fig. 5b), the influence of buildings on the wind field is diminished, which is mainly reflected by the fact that the wind directions at this height are more consistent to the background wind direction,~~ The phenomenon was also found in a ~~consisting with~~ previous ~~studies~~ study (Sui et al., 2016).

To clearly show the details of the wind field, a sub-domain A (Fig. 3a) with complex building structures is selected from the entire computational domain. The near-surface winds disperse or converge horizontally and ~~climb~~ rise or ~~fall~~ subsidence vertically with the building (Fig. 5c). During the climb or fall with the building, downwash winds with high wind speeds occurred (as shown in the red dashed circles). Due to the complexity of the building layout, local circulation is formed on the west side of the BSC monitoring site, making the airflow around the building on the south side of the station ~~pile up~~ accumulate and forms an obvious convergence area (Fig. ~~5d~~ 5c), which is not conducive to the air circulation and pollution ~~transport~~ diffusion (as shown in the red box).

3.2.2 The wind field characteristics under different background wind directions

Figure 6 shows the distributions of near-surface wind and its divergence under four different background wind directions. In general, the overall wind direction in the area is consistent with the background wind direction, but the airflow near-surface is significantly affected by the building layout, ~~and thus formed~~ forming local circulations with ~~dispersion divergence and or~~ convergence zones. The wind speeds in the areas with dense buildings are significantly smaller than those in open areas (Figs. 6a-1, 6b-1, 6c-1, and 6d-1), which is attributed to the obvious frictional dragging effect of the dense buildings. The overall wind direction ~~of in~~ the area is generally the same as the background wind direction, but the airflow is ~~dispersed diverged~~ or converged by the influence of the building layout, resulting in a great difference ~~between the in~~ wind direction inside the block ~~and from~~ the background ~~wind direction~~. When the background wind direction is north or west (Figs. 6b and 6c), the overall wind speed in the area is relatively large. This is mainly due to the temperate monsoon climate in Zhengzhou, where northwest and west winds prevail in winter and wind speeds are relatively high. ~~The wind speed inside the block is smaller than the background wind speed, which is attributed to the obvious frictional dragging effect of the dense buildings on the flow field.~~

~~The~~ It is found that the windward side of the building is mostly a divergence zone and the leeward side is mainly a convergence zone, which is more obvious for higher buildings. When the airflow meets the building, the airflow on the windward side of the building is blocked and thus spreads outward, forming a ~~dispersion divergence~~ zone; while the airflow on the leeward side of the building converges and generates a vortex

with lower wind speed, forming a convergence zone. ~~For example, Take the building~~
360 ~~where the~~ BSC monitoring site ~~is located as an example~~, when the background wind
direction is west, the wind speed on the windward side of the building is higher and
diffused outward by the building blockage (Fig. 6c-2), resulting in a significant
divergence zone (Fig. 6c-3). High-rise buildings have a greater impact on the wind field
and cause a strong degree of convergence and divergence. It can be seen that the degree
365 of divergence or convergence around the high-rise building is more significant than those
around low buildings in the area (Figs. 6b-3, 6c-3, and 6d-3). In addition, ~~It can be seen~~
~~that~~ the ventilation is better when the dominant airflow is in the same direction as
building layout (Fig. 6c). In the process of urban construction, the influence of prevailing
wind direction on the layout of buildings should be considered, which could effectively
370 improve the efficiency of urban ventilation.

3.3 Potential impact of ~~a~~ traffic sources

In this section, the S-TRACK system is used to analyze ~~the~~ potential impact of ~~a~~ main
traffic roads (R1-R4) in sub-domain B (Fig. 3a) on several receptor sites nearby with
different heights and locations with a number of schools and residential areas. The
375 widths of roads R1-R4 are about 45, 33, 20 and 18 meters, respectively. During January
2019, the average traffic volumes were about 2300 (R1), 490 (R2), 400 (R3) and 90 (R4)
cars per hour, respectively. Since the detailed information on road traffic emissions was
not available, the road traffic emissions were assumed to be uniformly distributed and
with identical intensity in this study. During the backward trajectory simulation, the
380 particles as long as passing within 5 m height above the road is considered to be a

~~potential contribution from the road emissions to the receptor site. January 2019 was selected as the simulation period. The sub-domain B includes a number of schools and residential areas.~~ Additionally, potential impact of traffic source under different background wind directions was also explored. The residence-time analysis (RTA), which has been previously used to identify the accounted contribution of emission sources to air quality of receptors (Yu, 2017; Salvador et al., 2008; Hopke et al., 2005; Poirot et al., 2001; Ashbaugh et al., 1985), was selected in this study to assess the potential contribution ratio of the traffic source on receptors. The RTA is expressed as:

$$R_{i,j} = \frac{\tau_{i,j}}{t} \quad (4)$$

where $R_{i,j}$ indicates the contribution ratio of the grid (i,j) to receptor; $\tau_{i,j}$ means the residence time in the grid (i,j) and t means the total residence time in all grids.

3.3.1 Potential impact of traffic source at different sites in winter

In order to analyze the potential impact of the traffic source on different locations, the receptor sites were selected at different locations and heights, and the overall potential contribution ratio of all wind directions for January 2019 was calculated by RTA (Table 4).~~as listed in Table 3.~~ Receptor sites S2-S8, with identical horizontal location but different heights, are selected to investigate contributions of traffic source to receptor sites at different heights. The potential contribution ratios of all the four roads are 4.05%, 4.25%, 4.33%, and 4.67% for receptor sites S2 to S5, with the height of 2 m, 5 m, 10 m, and 15 m, respectively. However, as the receptor height continues to rise, namely from S5 to S8, the potential contribution ratios of the roads gradually decrease

405 from 4.67% to 3.55% (Table 4). It's noteworthy that the contributions from R1 and R3 are primary, especially the R1, which may be due to the closer distance to the site and the generally northeast wind field. The potential impact of the traffic source is the greatest when the receptor site is located at a height of 15 m, suggesting the air quality at that height is most susceptible to traffic emissions under the northeast wind field. In addition, according to density distribution of all trajectory points that have passed through the traffic roads (Figs. 7), it can be seen that the road section with large potential impact to the receptor sites generally located to their northeast, which might be a result of the combination effect of the background wind field and the building layout. For more details, the vertical structure of winds along the direction of the wind field at the receptor site S2 (Fig. 8b) is also presented. It can be seen that there is a general upward motion in the airflow, making the position with the greatest potential contribution ratio from traffic source locate at a certain height, which is about 15 m over the receptor site S2 in this case.

415
420 It can be seen from Table 4 that R1 is the road with the greatest potential impact to the receptor sites. The horizontal distance between road R1 and the receptor sites is about 300 m and the peak of the potential contribution ratios occurs at a height of about 15 m (corresponding to the site S5). However, for the road R3, which is closest to the receptor sites in horizontal (about 200 m), the contribution ratios are lower than those of the road R1. Figure 8a shows that the near ground winds are generally northeast, resulting in that the probability of traffic contributions from R1 and R3 road sections upwind of the site S2 is roughly the same. Nonetheless, as mentioned in section 3.3, the width for the road R1 was about twice of that for the road R3. Therefore, even R1 was a little farther from

425 the receptor sites than R3, the contribution ratios of R1 to the sites were calculated larger
than those of R3. For the R2 and R4, the distance from the receptor sites is about 1200
and 1500 m, respectively, far away than those of R1 and R3. In addition, under the
northeast winds, traffic source was hardly transported to the receptor sites, rendering the
contribution ratios quite small below 50 m (Table 4). It can also be seen, from Table 4,
430 that the corresponding potential contribution ratios of R2 and R4 may peak at a height
over 50 m.

Since the road R1 had the largest potential contribution to the receptor sites, the
contribution of R1 to different positions is focused in the subsequent discussion. For the
receptor site S1, which is about 400 m from the ~~traffic road~~R1, located in a dense
435 building area with the building height at 30 to 40 meters, the potential contribution ratio
of the traffic source on the receptor site ~~was~~is calculated to be 1.81%. For the receptor
site S2, which is about 300 m from the traffic road, located in an open area and
surrounded by low buildings, the potential contribution ratio of the traffic source is
determined to be 2.38%. It might be inferred that the wind field difference partially
440 resulted from the influence of buildings layout ~~leads~~ to the higher contribution ratio ~~to~~
S2. ~~Additionally, the difference in the wind environment at different locations might be~~
~~another influence factor for the difference.~~From the average wind field in January 2019
(Fig.8a), it can be seen that the winds were influenced by high-rise buildings around the
S1, resulting in a change in transport path of pollutants and thus, making pollutants
445 difficult to reach the S1 site. However, for S2 site, the winds were less influenced by the
buildings and pollutants were more easily transported there.

Receptor sites S2-S8 are selected to investigate differences in contributions of traffic source to receptor sites at different heights. The potential contribution ratios of the road are 2.38%, 2.57%, 2.71%, and 2.98% for receptor sites S2 to S5, with the height of 2 m, 5 m, 10 m, and 15 m, respectively (Table 3). However, as the receptor height continues to rise, namely from S5 to S8, the potential contribution ratio of the road gradually decreases from 2.98% to 1.94%. The potential impact of the traffic source is the greatest when the receptor site is located at a height of 15 m, suggesting the air quality at that height is most susceptible to traffic emissions when the building is approximately 400 meters from traffic road. In addition, from density distribution of all trajectory points that have passed through the traffic road (Figs. 7), it can be seen that the road section with larger potential impact to air pollution at receptor sites is both located to their northeast, which might be a result of the combination effect of the background wind field and the building layout.

3.3.2 Potential impact of traffic source under different background wind directions

In order to investigate the potential impact of traffic source under different background wind directions, the receptor site S2 influenced by the R1 under the east, the south, the west, and the north wind directions was classified from the simulation period ~~(not shown)~~. The potential contribution ratios of traffic source were ~~calculated~~ estimated to be 2.45%, 0.07%, 1.98%, and 2.97% for the east, the south, the west, and the north wind directions, respectively, revealing that the difference in potential impact ~~is~~ was largest between the south and north wind directions. When the background wind direction ~~is~~ was south, the receptor site ~~is~~ was located upwind of the road, and the road

470 traffic source contributed~~s~~ very little to the receptor site. On the contrary, when the receptor site ~~is-was~~ downwind of the road ~~when the wind direction is~~with northern winds, ~~and~~ the contribution ratio of road traffic source to the receptor site ~~was~~is the greatest. When the background wind direction ~~was~~is east and west, the contribution ratio to the receptor point ~~was~~is similar, ~~and lies-ranging~~ between the ratios~~-that~~ under south and north wind directions. The ~~higher-lower~~ contribution ratio during westerly winds 475 relatively to that under easterly winds ~~may-might~~ partially be due to the denser distribution of buildings upwind of the receptor site. Complex building layouts changed the structure of the wind field and thus had an impact on the transport of pollutants. The slow air circulation in dense building areas made it unfavourable for pollutants to be transported. In the windward side of the dense building area, the wind was blocked and 480 diverted to both sides of the building. Pollutants were difficult to transport to the leeward side of the building, where the receptor site was located. The results of the potential impact of traffic source under different background wind conditions is helpful to understand the street-level pollution transport characteristics and provides~~s~~ effective suggestions for the traffic pollution control strategies.

485 4. Conclusions

A street-level pollutant tracking system ~~was~~has been developed to simulate micro-scale meteorology and used to analy~~se~~ze the characteristics of wind environment and the potential traffic source contribution of air pollution to receptors through backward simulations in a city district. In general, the S-TRACK system is effective in simulating 490 the street-level meteorological and pollution problems. The presence of buildings has a

significant effect on the wind environment, i.e., the dragging effect of dense buildings renders the wind speed inside the block smaller than the background wind speed. The ventilation is better when the dominant airflow is consistent with the direction of building layout. Influenced by the building layout, the airflow near-surface is formed with divergence and convergence zones. The windward side of the building is mostly a divergence zone and the leeward side is mostly a convergence zone, which is more obvious for higher buildings.

As a test case, the S-TRACK system has been used to investigate the potential impact of ~~a~~ traffic source on receptor sites with different locations, heights and background wind directions in a city district. ~~The method of RTA was used to assess the potential impact of traffic sources on receptor air quality.~~ The potential impact of traffic sources on a specific receptor site varies under different background wind directions, which ~~were~~ are estimated to be 2.45%, 0.07%, 1.98%, and 2.97% for the east, the south, the west, and the north wind directions, respectively. The difference in potential contribution under east and west wind directions might partially be due to the density of buildings upwind of the receptor site. For a specific location of this case study, the potential traffic contribution ratios also varied with height at about ~~4.052.38%~~, ~~2.574.25%~~, ~~2.714.33%~~, ~~2.984.67%~~, ~~2.754.38%~~, ~~2.303.64%~~ and ~~1.943.55%~~ at for 2, 5, 10, 15, 20, 40, 50 m, respectively, manifesting a significant trend of increasing and then decreasing with height. In addition, the height of position with the greatest potential contribution ratio from the traffic source varies jointly influenced by the distance between the position and traffic source, as well as the background wind field.

In the future, ~~more-in-depth~~ simulation experiments with different building layouts, wind field environments, and distances between traffic source and receptor are required to ~~study-quantify~~ the potential impact of street-level pollution sources ~~-in-depth~~. ~~In addition, due to the unavailability of street level emissions in the Jinshui district, further quantitative impact analysis of traffic sources could not be conducted in this study.~~ ~~Future in-depth investigations of~~ and to establish the relationship between meteorological conditions, buildings and various emissions (point, area and line sources) in the street-level ~~are also needed as a better theoretical basis and practical suggestions for~~ an effective management of regional pollution in a city.

Appendix

1. Some settings to improve the calculations efficiency of CFD

It is true that using a CFD model for the atmospheric numerical simulation has the problem of high computational cost. In this study, the RANS is chosen as the CFD preprocessing model, which requires relatively small amount of computational resources. The time step of STAR-CCM+ is set to 60s, with a maximum of 20 internal iterations in each time step and a parallel computing with 32 CPUs is done on a supercomputer. The simulation error increases with the simulation time. In order to ensure the efficiency and accuracy of the simulation, the month was divided into four time periods to simulate, as shown in Table A1.

Table A1. The division of each simulation time period and the physical time spent on the simulation

<u>Simulation start time</u>	<u>Simulation end time</u>	<u>Length of simulation time</u>	<u>Physical time spent</u>
------------------------------	----------------------------	----------------------------------	----------------------------

<u>2018/12/31 00:00:00</u>	<u>2019/1/ 09 04:00:00</u>	<u>220h</u>	<u>126.45h</u>
<u>2019/1/08 00:00:00</u>	<u>2019/1/ 17 04:00:00</u>	<u>220h</u>	<u>128.33h</u>
<u>2019/1/ 16 00:00:00</u>	<u>2019/1/25 04:00:00</u>	<u>220h</u>	<u>128.53h</u>
<u>2019/1/24 00:00:00</u>	<u>2019/2/01 08:00:00</u>	<u>200h</u>	<u>117.10h</u>

2. Significance test

535 Significance test is used to determine the significance of the results in relation to the null hypothesis, with a p-value, or probability value describing how likely the data would have occurred by random chance (i.e. that the null hypothesis is true). A p-value less than 0.05 (typically ≤ 0.05) is statistically significant. It indicates strong evidence against the null hypothesis, as there is less than a 5% probability the null is correct.

540 3. The observed data for January 2019 at various meteorological stations in Zhengzhou city.

Table A2. The location of each meteorological station and the average wind speed.

<u>number</u>	<u>Latitude and longitude coordinates</u>	<u>Average wind speed</u>
<u>1</u>	<u>(34.7274 N, 113.7493 E)</u>	<u>0.92 m s⁻¹</u>
<u>2</u>	<u>(34.73506 N, 113.6457 E)</u>	<u>0.92 m s⁻¹</u>
<u>3</u>	<u>(34.7466 N, 113.6876 E)</u>	<u>1.32 m s⁻¹</u>
<u>4</u>	<u>(34.76117 N, 113.6883 E)</u>	<u>0.61 m s⁻¹</u>
<u>5</u>	<u>(34.78245 N, 113.6567 E)</u>	<u>1.51 m s⁻¹</u>
<u>6</u>	<u>(34.81151 N, 113.6948 E)</u>	<u>1.48 m s⁻¹</u>
<u>7</u>	<u>(34.83267 N, 113.5453 E)</u>	<u>0.72 m s⁻¹</u>

545 4. Divergence

The divergence is a quantity that describes the degree to which air converges from its surroundings to a point or flows away from a point. It is used to describe the intensity of divergence and convergence at locations in space. The formula is as follows.

$$\underline{\underline{div \mathbf{v} = \nabla \cdot \mathbf{v} = \frac{\partial u}{\partial x} + \frac{\partial v}{\partial y} + \frac{\partial w}{\partial z}}}$$

550 where u , v and w are the components of the wind in the x , y and z direction, respectively.

When the $div \mathbf{v} < 0$, the location is convergence; when the $div \mathbf{v} > 0$, the location is divergence.

5. PBLH validation

The bulk Richardson number (Ri) method was taken to estimate the BLH base on the sounding data of Zhengzhou. Ri is expressed as:

$$\underline{\underline{R_i(z) = \frac{(g/\theta_{vs})(\theta_{vz} - \theta_{vs})(z - z_s)}{(u_z - u_s)^2 + (v_z - v_s)^2 + (bu_*^2)^2}}}$$

where z is the height above ground, s the surface, g means the acceleration of gravity, θ the virtual potential temperature, u and v the component of wind speed, and u the surface friction velocity. u can be ignored here due to it is small relative to the wind shear (Vogelezang and Holtslag, 1996). Previous theoretical and laboratory studies suggested that when Ri is smaller than a critical value (~ 0.25), the laminar flow becomes unstable (Stull, 1988). Therefore, the lowest level z at which the interpolated Ri exceeds the critical value of 0.25 is referred to as PBLH in this study, which is referred to the criterion used by Seidel et al. (2012). The R value is 0.57, passed the 99% significance test. It can be seen from Figure A1 that the variation of boundary layer height is generally captured.

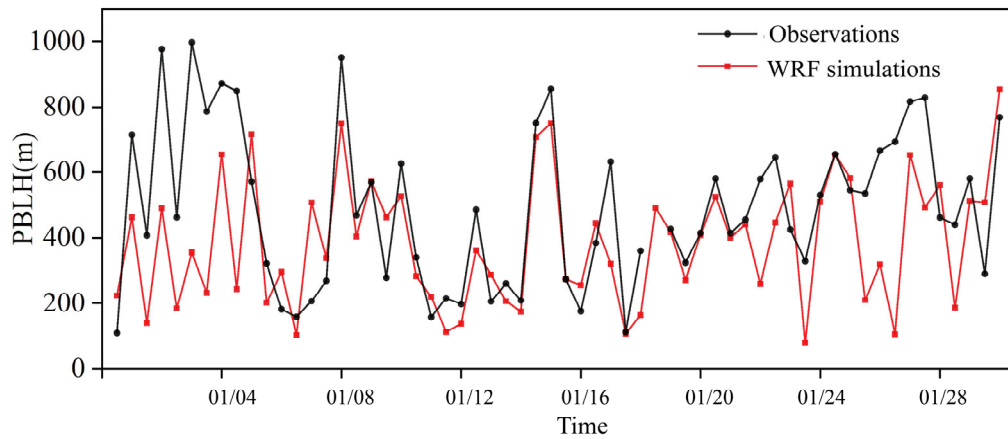


Figure A1. Time series of the observed (black) and simulated (red) PBLH at 8:00 and 20:00 Beijing time (BJT) in Zhengzhou sounding site.

570

Code/data availability

All source code and data can be accessed by contacting the corresponding authors Sunling Gong (gongsl@cma.gov.cn) and Lei Zhang (leiz09@cma.gov.cn).

Authors contribution

575 Sunling Gong and Lei Zhang designed the research. Huan Zhang performed the simulations and wrote the manuscript with suggestions from all authors. Jingyue Mo, Huabing Ke, and Shuhua Lu assisted with data processing. Jianjun He, Yaqiang Wang and Lixin Shi participated in the scientific interpretation and discussion. All authors contributed to the discussion and improvement of the manuscript.

580 Competing interests

The authors declare that they have no conflict of interest.

Acknowledgments

The authors would like to acknowledge Bin Cui and Lin Zhang from Peking University and Liangfu Chen from Chinese Academy of Sciences for their valuable suggestions to
585 improve the article.

References

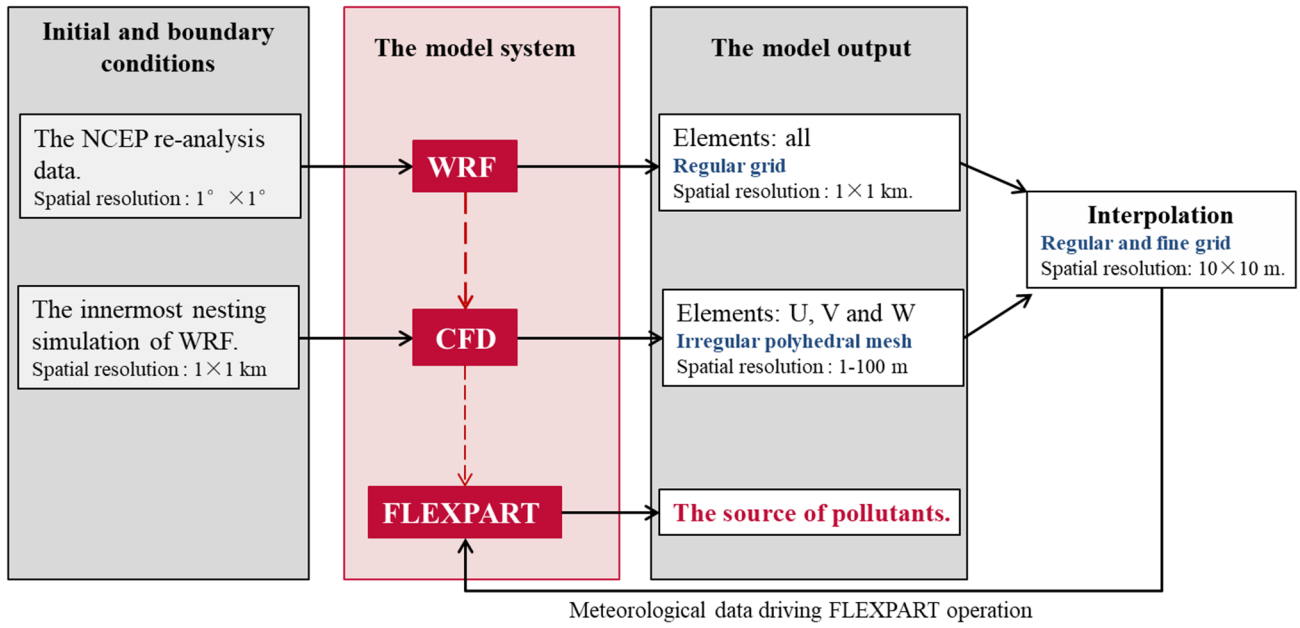
- Ashbaugh, L., Malm, W., and Sadeh, W.: A residence time probability analysis of sulfur concentrations at grand Canyon national park, *Atmos. Environ.*, 19, 1263-1270, [https://doi.org/10.1016/0004-6981\(85\)90256-2](https://doi.org/10.1016/0004-6981(85)90256-2), 1985.
- 590 Aynsley, R.: Politics of pedestrian level urban wind control, *Build Environ*, 24, 291-295, [https://doi.org/10.1016/0360-1323\(89\)90022-X](https://doi.org/10.1016/0360-1323(89)90022-X), 1989.
- [Borge, R., Jose Luis Santiago, David de la Paz, Fernando Martín, Jessica Domingo, Cristina Valdés, Beatriz Sánchez, Esther Rivas, Ma Teresa Rozas, Sonia Olaechea Lázaro, Pérez, J., and Fernández, a. A. L.-P.: Application of a short term air quality action plan in Madrid \(Spain\) under a high-pollution episode - Part II: Assessment from multi-scale modelling. *Sci. Total Environ.*, 635, 1574-1584, <https://doi.org/10.1016/j.scitotenv.2018.04.323>, 2018.](#)
- 595 Brioude, J., Arnold, D., Stohl, A., Cassiani, M., Morton, D., Seibert, P., Angevine, W., Evan, S., Dingwell, A., Fast, J. D., Easter, R. C., Pisso, I., Burkhardt, J., and Wotawa, G.: The Lagrangian particle dispersion model FLEXPART-WRF version 3.1, *Geosci. Model Dev. (GMD)*, 6, 1889-1904, <https://doi.org/10.5194/gmd-6-1889-2013>, 2013.
- Carvalho, D., Rocha, A., Gómez-Gesteira, M., and Santos, C.: A sensitivity study of the WRF model in wind simulation for an area of high wind energy, *Environ. Model. Software*, 33, 23-34, <https://doi.org/10.1016/j.envsoft.2012.01.019>, 2012.
- 600 Cécé, R., Bernard, D., Brioude, J., and Zahibo, N.: Microscale anthropogenic pollution modelling in a small tropical island during weak trade winds: Lagrangian particle dispersion simulations using real nested LES meteorological fields, *Atmos. Environ.*, 139, 98-112, <https://doi.org/10.1016/j.atmosenv.2016.05.028>, 2016.
- Chen, F. and Dudhia, J.: Coupling an Advanced Land Surface-Hydrology Model with the Penn State-NCAR MM5 Modeling System. Part I: Model Implementation and Sensitivity, *Mon. Weather Rev.*, 129, 569-585, [https://doi.org/10.1175/1520-0493\(2001\)129<0569:CAALSH>2.0.CO;2](https://doi.org/10.1175/1520-0493(2001)129<0569:CAALSH>2.0.CO;2), 2001.
- 605 de Foy, B., Burton, S. P., Ferrare, R. A., Hostetler, C. A., Hair, J. W., Wiedinmyer, C., and Molina, L. T.: Aerosol plume transport and transformation in high spectral resolution lidar measurements and WRF-Flexpart simulations during the MILAGRO Field Campaign, *Atmos. Chem. Phys.*, 11, 3543-3563, <https://doi.org/10.5194/acp-11-3543-2011>, 2011.
- 610 Ehrhard, J., Khatib, I., Winkler, C., Kunz, R., Moussiopoulos, N., and Ernst, G.: The microscale model MIMO: development and assessment, *J. Wind. Eng. Ind. Aerodyn.*, 85, 163-176, [https://doi.org/10.1016/S0167-6105\(99\)00137-3](https://doi.org/10.1016/S0167-6105(99)00137-3), 2000.
- Fast, J. D. and Easter, R. C.: A Lagrangian particle dispersion model compatible with WRF, 7th WRF Users Workshop, NCAR, 19-22, 2006.
- Fernando, H., Zajic, D., Sabatino, S. D., Dimitrova, R., and Dallman, A.: Flow, turbulence, and pollutant dispersion in urban atmosphere, *Phys. Fluids*, 22, 051301, <https://doi.org/10.1063/1.3407662>, 2010.
- 615 Gao, Y., Shan, H., Zhang, S., Sheng, L., Li, J., Zhang, J., Ma, M., Meng, H., Luo, K., Gao, H., and Yao, X.: Characteristics and sources of PM_{2.5} with focus on two severe pollution events in a coastal city of Qingdao, China, *Chemosphere*, 247, 125861, <https://doi.org/10.1016/j.chemosphere.2020.125861>, 2020.
- Gosman, A. D.: Developments in CFD for industrial and environmental applications in wind engineering, *J. Wind. Eng. Ind. Aerodyn.*, 81, 21-39, [https://doi.org/10.1016/S0167-6105\(99\)00007-0](https://doi.org/10.1016/S0167-6105(99)00007-0), 1999.
- 620 He, J., Mao, H., Gong, S., Yu, Y., and Zou, C.: Investigation of particulate matter regional transport in Beijing based on numerical simulation, *Aerosol Air Qual. Res.*, 17, 1181-1189, <https://doi.org/10.4209/AAQR.2016.03.0110>, 2017a.
- He, J., Zhang, L., Yao, Z., Che, H., Gong, S., Wang, M., Zhao, M., and Jing, B.: Source apportionment of particulate matter based on numerical simulation during a severe pollution period in Tangshan, North China, *Environ. Pollut.*, 266, 115133, <https://doi.org/10.1016/j.envpol.2020.115133>, 2020.
- 625 He, J. J., Yu, Y., Liu, N., Zhao, S. P., and Chen, J. B.: Impact of land surface information on WRFs performance in complex terrain area, *Chin. J. Atmos. Sci.*, 38, 484-498, <https://doi.org/10.3878/j.issn.1006-9895.2013>, 2014.
- He, J. J., Yu, Y., Yu, L. J., Liu, N., and Zhao, S. P.: Impacts of uncertainty in land surface information on simulated surface temperature and precipitation over China, *Int J Climatol*, 37, 829-847, <https://doi.org/10.1002/joc.5041>, 2017b.
- 630 Hendricks, E. A., Diehl, S. R., Burrows, D. A., and Keith, R.: Evaluation of a Fast-Running Urban Dispersion Modeling System Using Joint Urban 2003 Field Data, *J Appl Meteorol Climatol*, 46, 2165-2179, <https://doi.org/10.1175/2006JAMC1289.1>, 2007.
- Heo, J., Foy, B. D., Olson, M. R., Pakbin, P., Sioutas, C., and Schauer, J.: Impact of regional transport on the anthropogenic and biogenic secondary organic aerosols in the Los Angeles Basin, *Atmos. Environ.*, 103, 171-179, <https://doi.org/10.1016/J.ATMOSENV.2014.12.041>, 2015.
- 635 Hopke, P., Zhou, L., and Poirot, R.: Reconciling trajectory ensemble receptor model results with emissions, *Environ. Sci. Technol.*, 39(20), 7980-7983, <https://doi.org/10.1021/es049816g>, 2005.
- Iacono, M. J., Delamere, J. S., Mlawer, E. J., Shephard, M. W., and Collins, W. D.: Radiative Forcing by Long-Lived Greenhouse Gases: Calculations with the AER Radiative Transfer Models, *J. Geophys. Res.-Atmos.*, 113, D13103, <https://doi.org/10.1029/2008JD009944>, 2008.
- 640 [Jls, A., Bse, A., Cq, B., Ddlp, B., Am, A., Fm, A., Rb, B., Er, A., Gm, A., and Ed, A.: Performance evaluation of a multiscale modelling system applied to particulate matter dispersion in a real traffic hot spot in Madrid \(Spain\) - ScienceDirect. *Atmospheric Pollut.*, 11, 141-155, <https://doi.org/10.1016/j.apr.2019.10.001>, 2020.](#)
- Kurppa, M., Hellsten, A., Auvinen, M., Raasch, S., Vesala, T., and Järvi, L.: Ventilation and Air Quality in City Blocks Using Large-Eddy SimulatioŽ Urban Planning Perspective, *Atmosphere*, 9, 65, <https://doi.org/10.3390/ATMOS9020065>, 2018.

- Kwak, K.-H., Baik, J.-J., Ryu, Y.-H., and Lee, S.-H.: Urban air quality simulation in a high-rise building area using a CFD model coupled with mesoscale meteorological and chemistry-transport models, *Atmos. Environ.*, 100, 167-177, <https://doi.org/10.1016/j.atmosenv.2014.10.059>, 2015.
- 650 Lei, L., Fei, H., Cheng, X. L., and Han, H. Y.: The application of computational fluid dynamics to pedestrian level wind safety problem induced by high-rise buildings, *Chin. Phys. B*, 13, 1070-1075, <https://doi.org/10.1088/1009-1963/13/7/018>, 2004.
- Lei, L. I., Yang, L., Zhang, L. J., and Jiang, Y.: Numerical Study on the Impact of Ground Heating and Ambient Wind Speed on Flow Fields in Street Canyons, *Adv Atmos Sci*, 29, 1227-1237, <https://doi.org/10.1007/s00376-012-1066-3>, 2012.
- 655 Li, L., Hu, F., Cheng, X. L., Jiang, J. H., and Ma, X. G.: Numerical simulation of the flow within and over an intersection model with Reynolds-averaged Navier-Stokes method, *Chin. Phys. B*, 15, 149-155, <https://doi.org/10.1088/1009-1963/15/1/024>, 2006.
- Li, S., Sun, X., Zhang, S., Zhao, S., and Zhang, R.: A Study on Microscale Wind Simulations with a Coupled WRF-CFD Model in the Chongli Mountain Region of Hebei Province, China, *Atmosphere*, 10, 731, <https://doi.org/10.3390/atmos10120731>, 2019.
- 660 Li, X.-X., Liu, C.-H., and Leung, D. Y. C.: Large-Eddy Simulation of Flow and Pollutant Dispersion in High-Aspect-Ratio Urban Street Canyons with Wall Model, *Bound. Layer Meteorol.*, 129, 249-268, <https://doi.org/10.1007/s10546-008-9313-y>, 2008.
- Lin, Y. L., Farley, R. D., and Orville, H. D.: Bulk Parameterization of the Snow Field in a Cloud Model, *J APPL METEOROL*, 22, 1065-1092, [https://doi.org/10.1175/1520-0450\(1983\)022<1065:BPOTSF>2.0.CO;2](https://doi.org/10.1175/1520-0450(1983)022<1065:BPOTSF>2.0.CO;2), 1983.
- 665 Liu, N., Yu, Y., He, J., and Zhao, S.: Integrated modeling of urban-scale pollutant transport: application in a semi-arid urban valley, Northwestern China (SCI), *Atmospheric Pollut. Res.*, 4, 306-314, <https://doi.org/10.5094/APR.2013.034>, 2013.
- Liu, S., Pan, W., Zhao, X., Zhang, H., Cheng, X., Long, Z., and Chen, Q.: Influence of surrounding buildings on wind flow around a building predicted by CFD simulations, *Build Environ*, 140, 1-10, <https://doi.org/10.1016/j.buildenv.2018.05.011>, 2018.
- 670 Macdonald, R. W., Griffiths, R. F., and Cheah, S. C.: Field experiments of dispersion through regular arrays of cubic structures, *Atmos. Environ.*, 31, 783-795, [https://doi.org/10.1016/S1352-2310\(96\)00263-4](https://doi.org/10.1016/S1352-2310(96)00263-4), 1997.
- Madala, S., Satyanarayana, A. N., Srinivas, C., and Kumar, M.: Mesoscale atmospheric flow-field simulations for air quality modeling over complex terrain region of Ranchi in eastern India using WRF, *Atmos. Environ.*, 107, 315-328, <https://doi.org/10.1016/J.ATMOSENV.2015.02.059>, 2015.
- 675 Mavroidis, I., Rf., G., and Dj., H.: Field and wind tunnel investigations of plume dispersion around single surface obstacles, *Atmos. Environ.*, 37, 2903-2918, [https://doi.org/10.1016/S1352-2310\(03\)00300-5](https://doi.org/10.1016/S1352-2310(03)00300-5), 2003.
- Milliez, M. and Carissimo, B.: Computational Fluid Dynamical Modelling of Concentration Fluctuations in an Idealized Urban Area, *Bound. Layer Meteorol.*, 127, 241-259, <https://doi.org/10.1007/s10546-008-9266-1>, 2008.
- 680 Nakanishi, M. and Niino, H.: An Improved Mellor-Yamada Level-3 Model: Its Numerical Stability and Application to a Regional Prediction of Advection Fog, *Bound. Layer Meteorol.*, 119, 397-407, <https://doi.org/10.1007/S10546-005-9030-8>, 2006.
- Nelson, M. A., Brown, M. J., Halverson, S. A., Bieringer, P. E., Annunzio, A., Bieberbach, G., and Meech, S.: A Case Study of the Weather Research and Forecasting Model Applied to the Joint Urban 2003 Tracer Field Experiment. Part 2: Gas Tracer Dispersion, *Bound. Layer Meteorol.*, 161, 461-490, <https://doi.org/10.1007/s10546-016-0188-z>, 2016.
- 685 Park, S. B., Baik, J. J., and Han, B. S.: Large-eddy simulation of turbulent flow in a densely built-up urban area, *Environ. Fluid Mech.*, 15, 235-250, <https://doi.org/10.1007/s10652-013-9306-3>, 2015.
- Poirot, R., Wishinski, P., Hopke, P., and Polissar, A.: Comparative application of multiple receptor methods to identify aerosol sources in northern Vermont, *Environ. Sci. Technol.*, 35(23), 4622-4636, <https://doi.org/10.1021/es011442t>, 2001.
- 690 Sada, K. and Sato, A.: Numerical calculation of flow and stack-gas concentration fluctuation around a cubical building, *Atmos. Environ.*, 36, 5527-5534, [https://doi.org/10.1016/S1352-2310\(02\)00668-4](https://doi.org/10.1016/S1352-2310(02)00668-4), 2002.
- Salvador, P., Artíñano, B., Querol, X., and Alastuey, A.: A combined analysis of backward trajectories and aerosol chemistry to characterise long-range transport episodes of particulate matter: the madrid air basin, a case study, *Sci. Total Environ.*, 390(2-3), 495-506, <https://doi.org/10.1016/j.scitotenv.2007.10.052>, 2008.
- 695 Sandeepan, B., Rakesh, P. T., and Venkatesan, R.: Numerical simulation of observed submesoscale plume meandering under nocturnal drainage flow, *Atmos. Environ.*, 69, 29-36, <https://doi.org/10.1016/J.ATMOSENV.2012.12.007>, 2013.
- [Santiago, J. L., Rafael Borge, Fernando Martín, David de la Paz, Alberto Martilli, Lumbreras, J., and Sánchez, a. B.: Evaluation of a CFD-based approach to estimate pollutant distribution within a real urban canopy by means of passive samplers., *Sci. Total Environ.*, 576, 46-58, https://doi.org/10.1016/j.scitotenv.2016.09.234, 2017.](https://doi.org/10.1016/j.scitotenv.2016.09.234)
- 700 [Schlünzen, K. H. and Sokhi, R. S.: Overview of Tools and Methods for Meteorological and Air Pollution Mesoscale Model Evaluation and User Training. Joint report by WMO and COST 728, WMO/TD-No. 1457, Geneva, Switzerland, 2008, 2008.](https://doi.org/10.1016/j.atmosenv.2008.08.018)
- Seidel, D. J., Zhang, Y., Beljaars, A., Golaz, J. C., Jacobson, A. R., and Medeiros, B.: Climatology of the planetary boundary layer over the continental United States and Europe, *Journal of Geophysical Research Atmospheres*, 117, <https://doi.org/10.1029/2012JD018143>, 2012.
- 705 [Stam, J.: Stable Fluids, *ACM Trans. Graph.*, 1999, https://doi.org/10.1145/311535.311548, 1999.](https://doi.org/10.1145/311535.311548)
- Steenburgh, W., J., Stoll, R., Gowardhan, A., Kochanski, A., K., Brown, and M., J.: One-Way Coupling of the WRF-QUIC Urban Dispersion Modeling System, *Journal of Applied Meteorology and Climatology*, *J Appl Meteorol Climatol*, <https://doi.org/10.1175/JAMC-D-15-0020.1>, 2015.
- 710 Stohl, A.: A backward modeling study of intercontinental pollution transport using aircraft measurements, *J. Geophys. Res.*, 108, 4370, <https://doi.org/10.1029/2002jd002862>, 2003.

Stohl, A. and James, P.: A Lagrangian Analysis of the Atmospheric Branch of the Global Water Cycle. Part I: Method Description, Validation, and Demonstration for the August 2002 Flooding in Central Europe, J Hydrometeorol, 5, 656, [https://doi.org/10.1175/1525-7541\(2004\)0052.0.CO;2](https://doi.org/10.1175/1525-7541(2004)0052.0.CO;2), 2004.

- 715 Stohl, A., Forster, C., Frank, A., Seibert, P., and Wotawa, G.: Technical note: The Lagrangian particle dispersion model FLEXPART version 6.2, Atmos. Chem. Phys., 5, 2461-2474, <https://doi.org/10.5194/ACP-5-2461-2005>, 2005.
- Stull, R. B.: An Introduction to Boundary Layer Meteorology, Springer Netherlands, Dordrecht, 1988.
- Sui, L., Jiang, M., Li, Z., and Zhou, S.: Diffusion effect analysis of pollution gas under the impact of urban three-dimensional pattern, in: 5th International Conference on Energy and Environmental Protection, Shengzhen, China, 17-18, September 2016, 903-909, 2016.
- 720 Temimi, M., Fonseca, R., Reddy, N. N., Weston, M., and Naqbi, H. A.: Assessing The Impact of Changes in Land Surface Conditions on WRF Predictions in Arid Regions, J Hydrometeorol, 21, 2829-2853, <https://doi.org/10.1175/JHM-D-20-0083.1>, 2020.
- Tewari, M., Kusaka, H., Chen, F., Coirier, W. J., Kim, S., Wyszogrodzki, A. A., and Warner, T. T.: Impact of coupling a microscale computational fluid dynamics model with a mesoscale model on urban scale contaminant transport and dispersion, Atmos. Res., 96, 656-664, <https://doi.org/10.1016/j.atmosres.2010.01.006>, 2010.
- 725 Vogelesang, D. and Holtslag, A.: Evaluation and model impacts of alternative boundary-layer height formulations, Bound.-Lay. Meteorol., 81, 245-269, <https://doi.org/10.1007/BF02430331>, 1996.
- Yu, C., Zhao, T., Bai, Y., Zhang, L., Kong, S., Yu, X., He, J., Cui, C., Yang, J., You, Y., Ma, G., Wu, M., and Chang, J.: Heavy air pollution with a unique “non-stagnant” atmospheric boundary layer in the Yangtze River middle basin aggravated by regional transport of PM_{2.5} over China, Atmos. Chem. Phys., 20, 7217-7230, <https://doi.org/10.5194/acp-20-7217-2020>, 2020.
- 730 Yu, T. Y.: Source identification of emission sources for hydrocarbon with backward trajectory model and statistical methods, Pol. J. Environ. Stud., 26(2), 893-902, <https://doi.org/10.15244/pjoes/65744>, 2017.
- Yucong, Miao, Shuhua, Liu, Hui, Zheng, Yijia, Zheng, Bicheng, and Chen: A multi-scale urban atmospheric dispersion model for emergency management, Adv Atmos Sci, 31, 13, <https://doi.org/10.1007/s00376-014-3254-9>, 2014.
- 735 Zhang, H., Xu, T., Zong, Y., Tang, H., Liu, X., and Wang, Y.: Influence of Meteorological Conditions on Pollutant Dispersion in Street Canyon, Procedia Engineering, 121, 899-905, <https://doi.org/10.1016/J.PROENG.2015.09.047>, 2015.
- Zhang, H., Tang, S., Yue, H., Wu, K., Zhu, Y., Liu, C.-J., Liang, B., and Li, C.: Comparison of Computational Fluid Dynamic Simulation of a Stirred Tank with Polyhedral and Tetrahedral Meshes, Iran. J. Chem. Chem. Eng., 39, 311-319, <https://doi.org/10.30492/IJCCE.2019.34950>, 2020.
- 740 Zheng, Y., Miao, Y., Liu, S., Chen, B., Zheng, H., and Wang, S.: Simulating Flow and Dispersion by Using WRF-CFD Coupled Model in a Built-Up Area of Shenyang, China, Adv. Meteorol, 2015, 1-15, <https://doi.org/10.1155/2015/528618>, 2015.

WRF-CFD-FLEXPART multi-model coupling simulation



The S-TRACK system

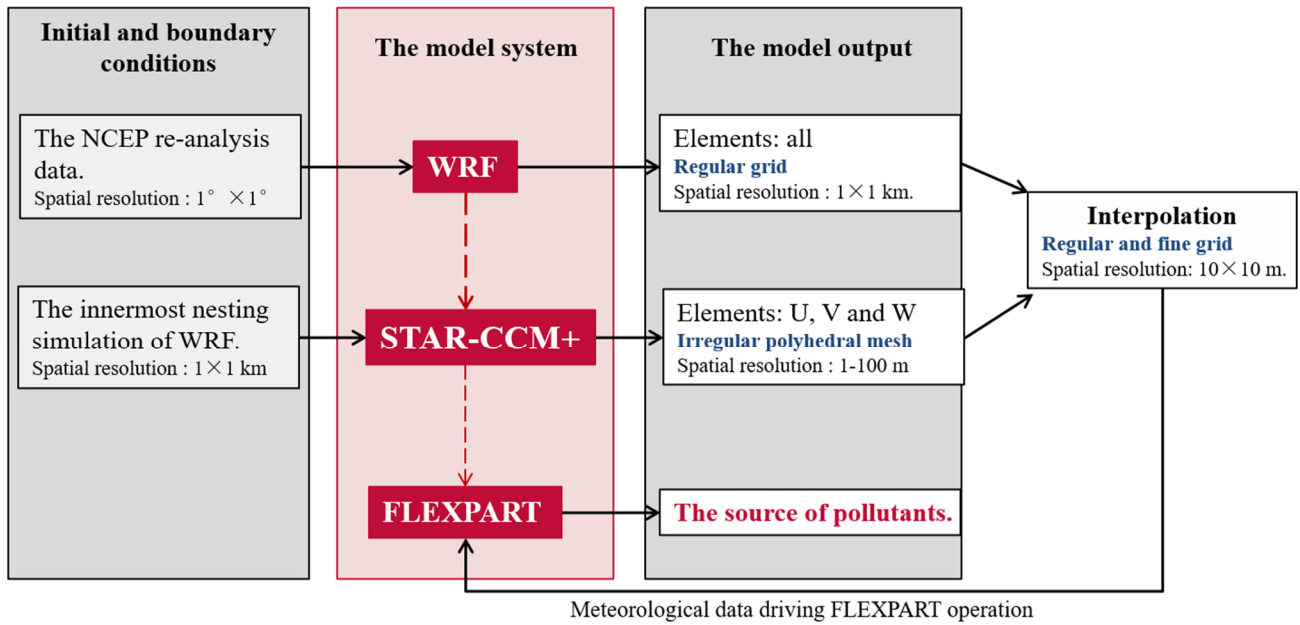
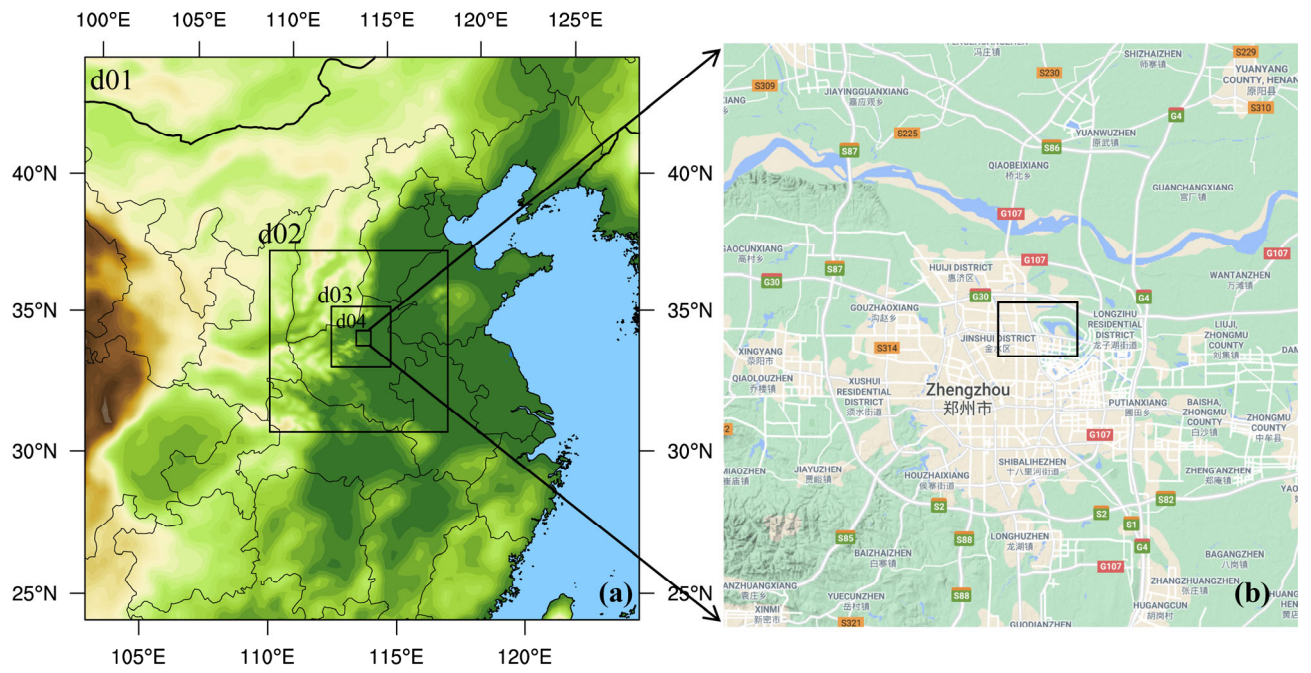
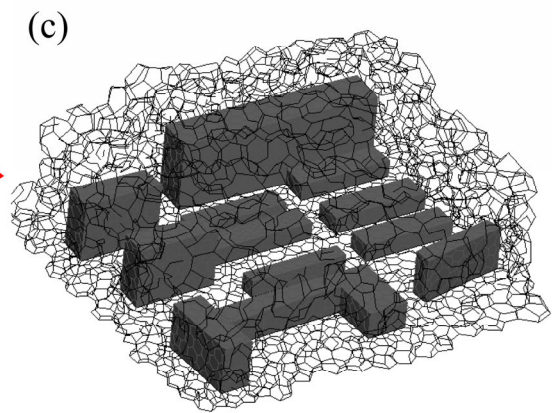
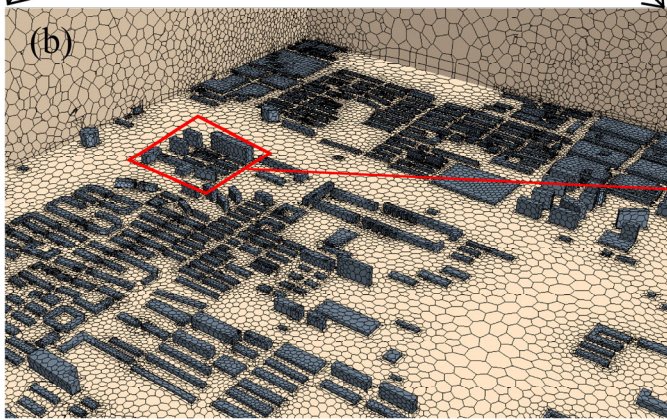
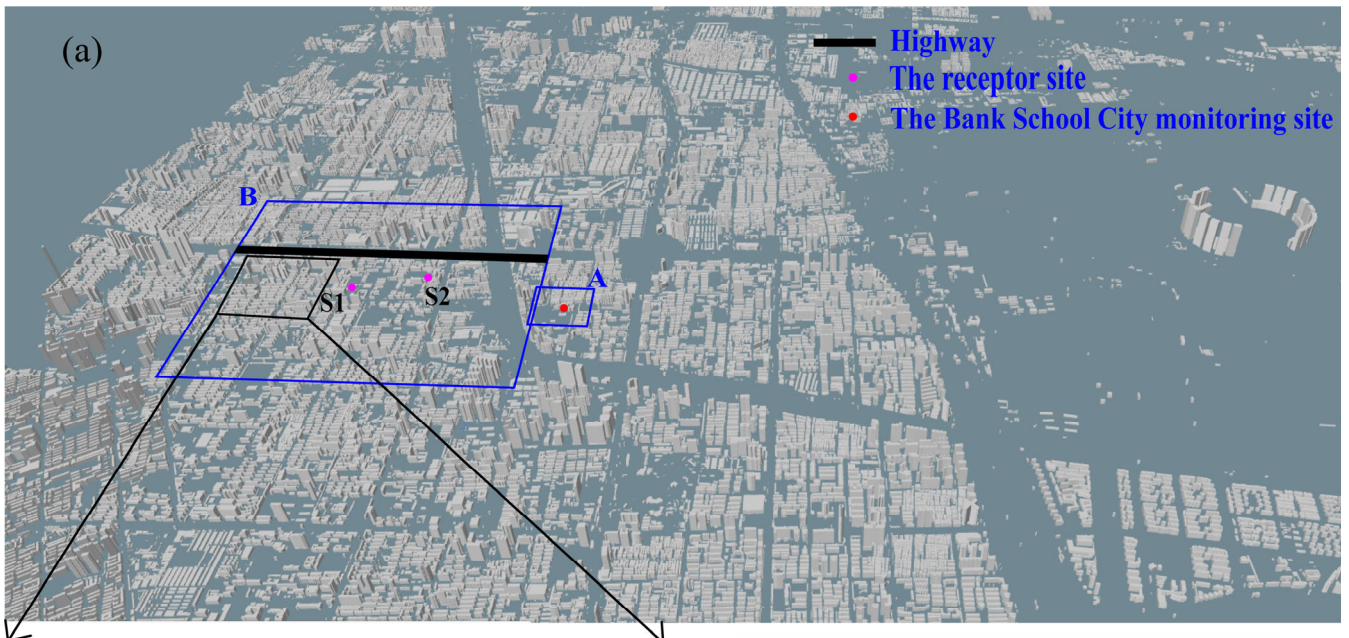


Figure 1: The S-TRACK system: The role of WRF, ~~CFD~~ STAR-CCM+ and FLEXPART in the S-TRACK system and the process of gradual refinement of resolution.



750

Figure 2: Domain configuration of the WRF model: (a) the range of the four nested domains (d1-d4); (b) the innermost nested domain (d4), within which the black box represents the CFD-STAR-CCM+ simulation domain (extracted from © Google Maps 2021).



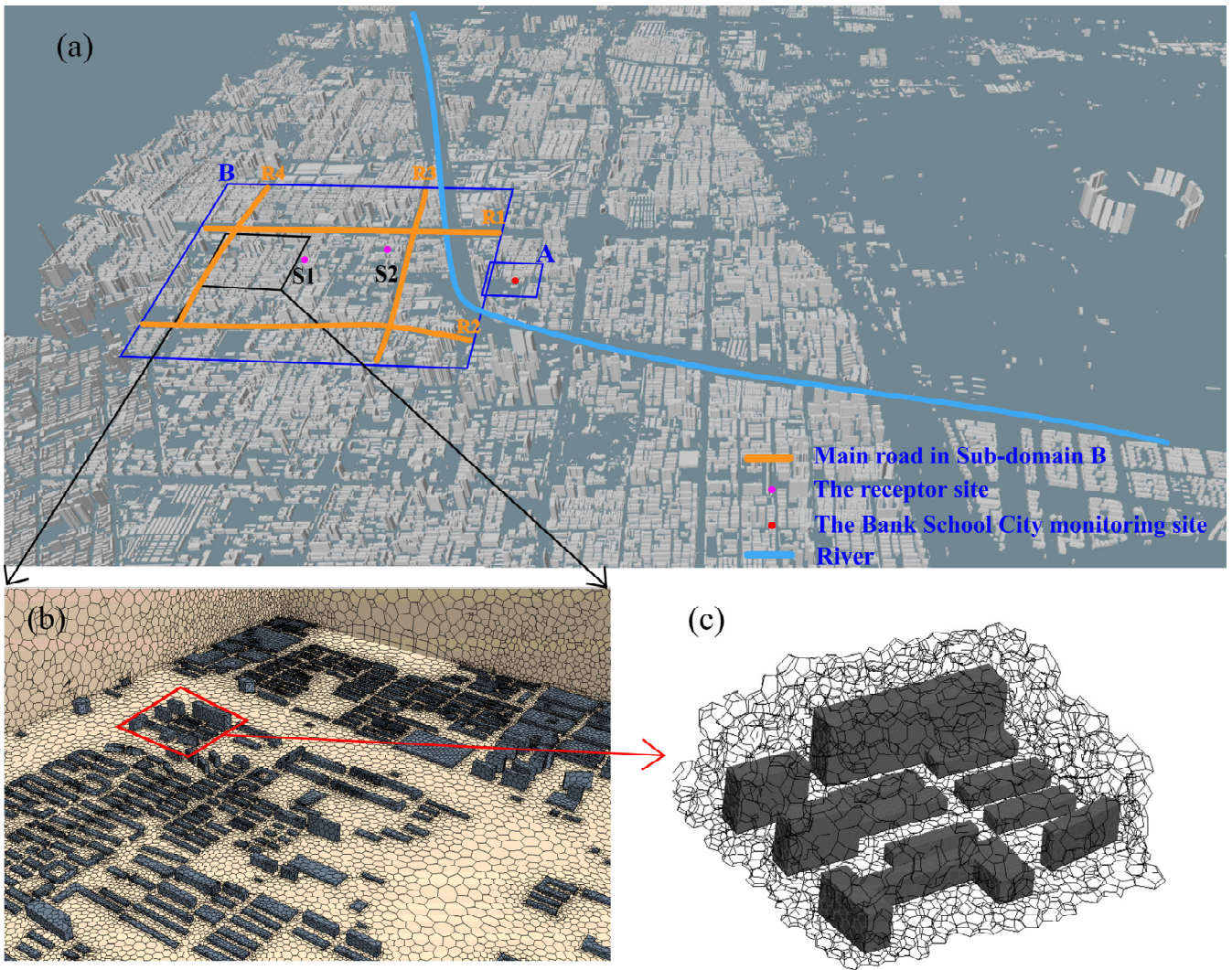


Figure 3: The computational domain of the **CFD-STAR-CCM+ model** is shown in (a). The sub-domain A is used for detailed analysis of the wind environment, and the Bank School City (BSC) monitoring site is marked with the red dot. Sub-domain B is used to analyze the potential impact of traffic source on receptor sites in the region, with magenta dots (S1 and S2) indicating the receptor sites and **Orange line indicating the main roads** a **black line indicating the highway**. The polyhedral mesh is used to divide the **CFD-STAR-CCM+ modeling simulation** area. The mesh details of the vertical cross section and building surface are shown in (b), and the 3D meshes are shown in (c).

760

765

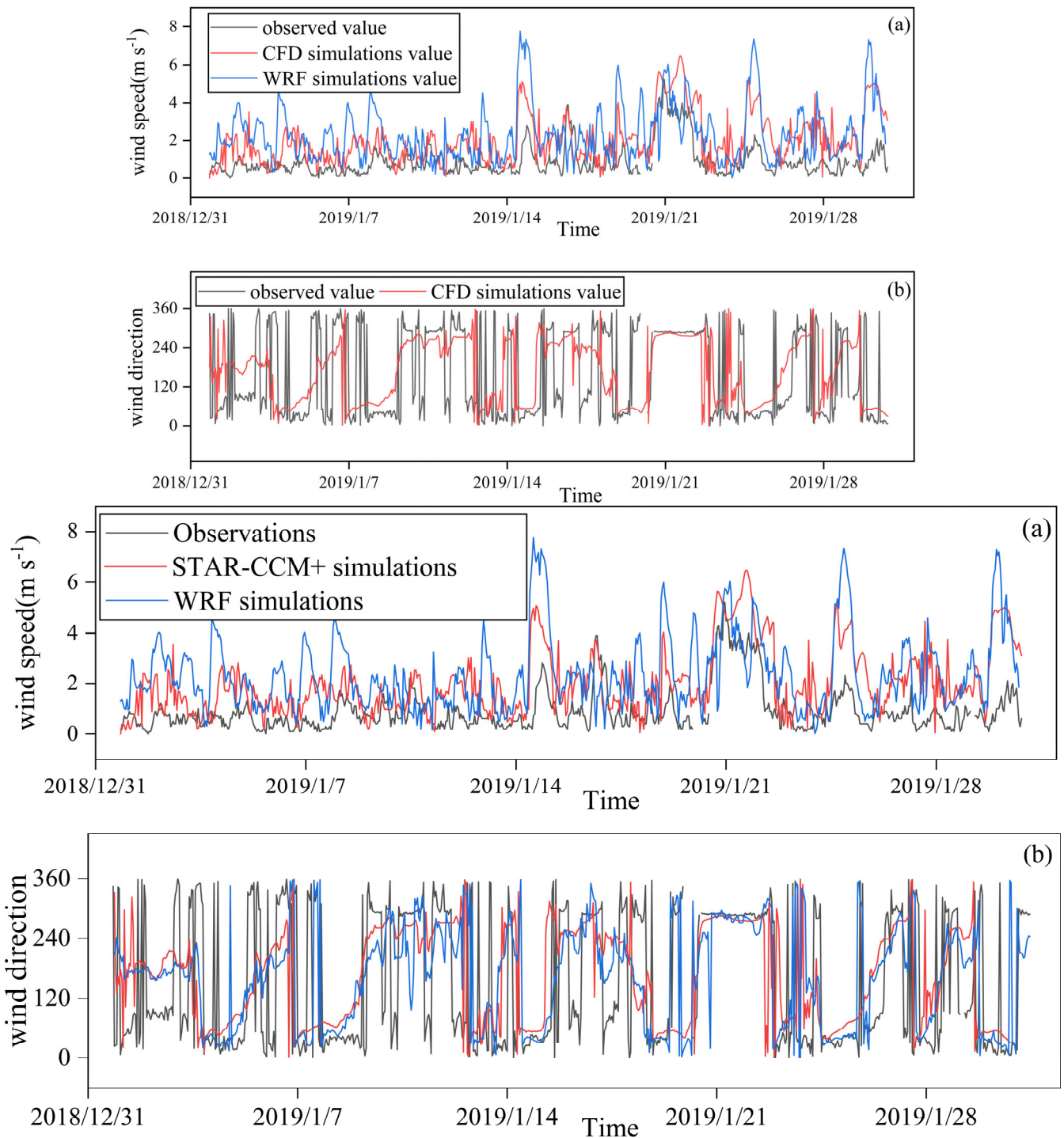
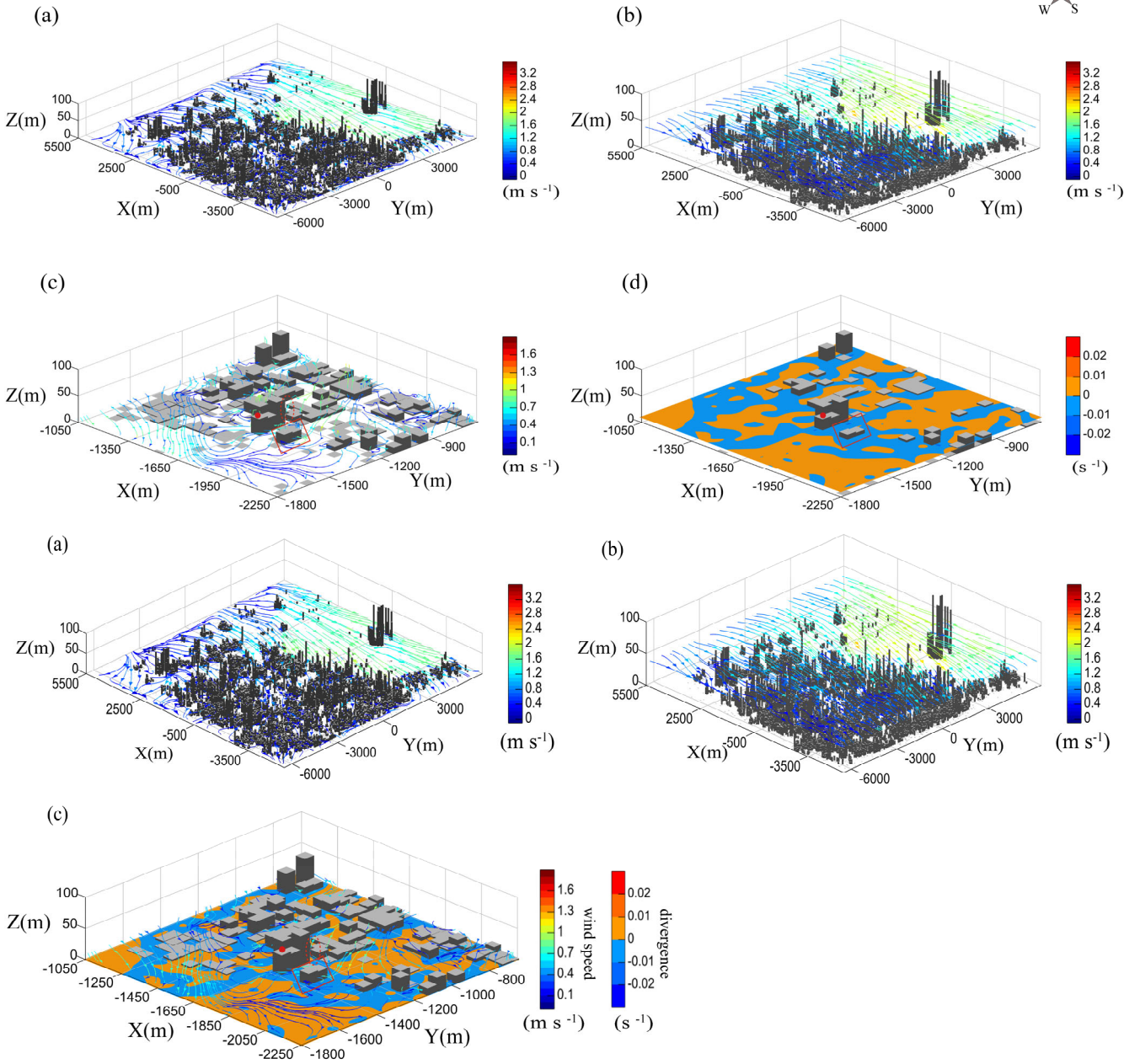
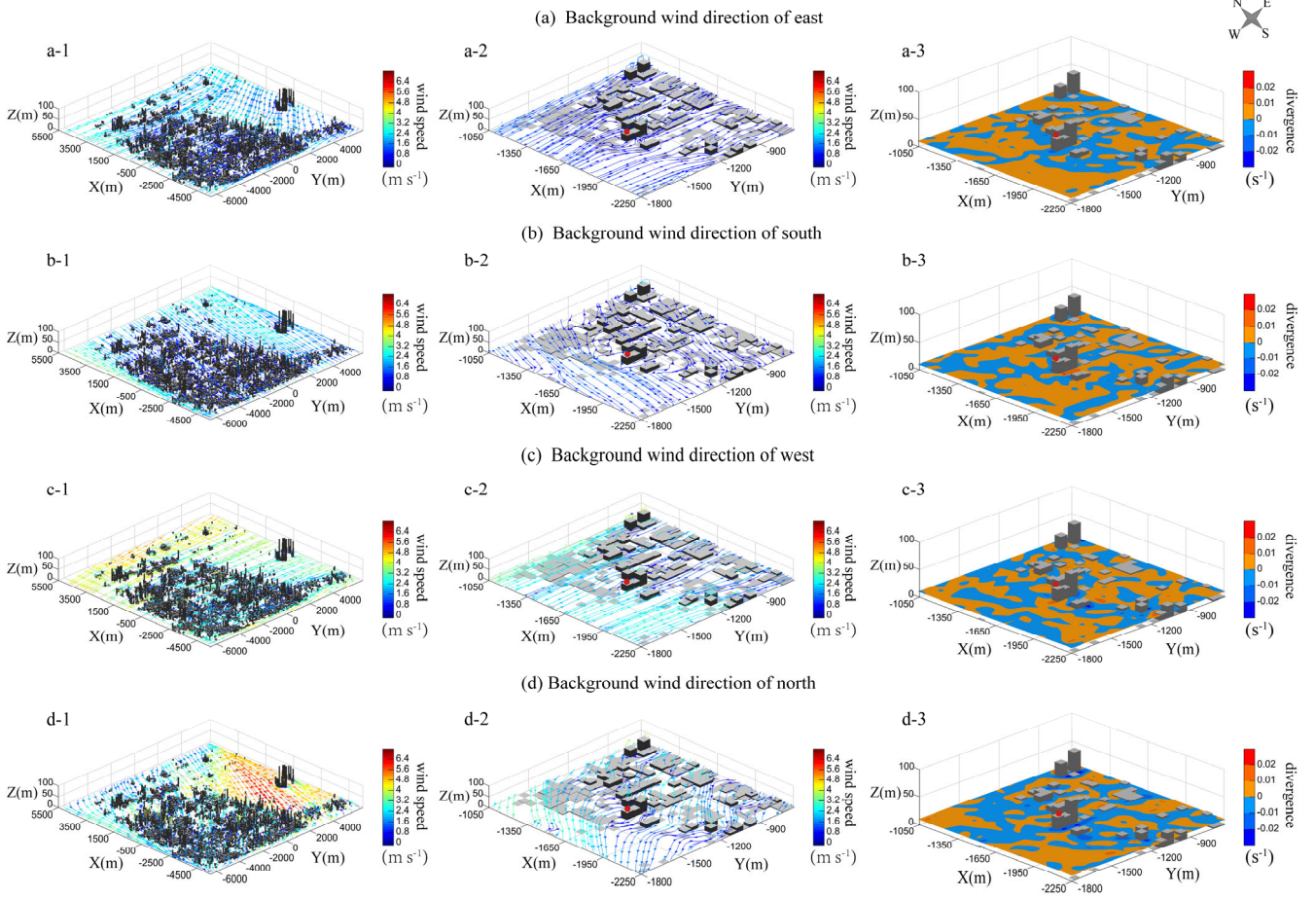


Figure 4: Evaluation of the wind simulation results at the BSC monitoring site (see in Fig. 3a): (a) the simulated, by WRF (blue line) and CFD-STAR-CCM+ (red line) model, respectively, and the observed (grey line) hourly near-surface wind speeds (a) and wind directions; (b) ~~the simulated, by CFD (red line), and observed (grey line) hourly near-surface wind directions.~~

770



775 **Figure 5:** The simulated wind streamlines at the height of 5 m (a) and 40 m (b) averaged in January 2019 in the whole S-TRACK simulation domain; the simulated wind streamlines (c) and divergence (d) at the near-surface averaged in January 2019 in the sub-domain A (see in Fig. 3a). The BSC monitoring site is marked with red dot.



780

Figure 6: The wind field streamlines and divergences under the background wind directions of east (a), south (b), west (c) and north (d). The BSC monitoring site is marked with red dot.

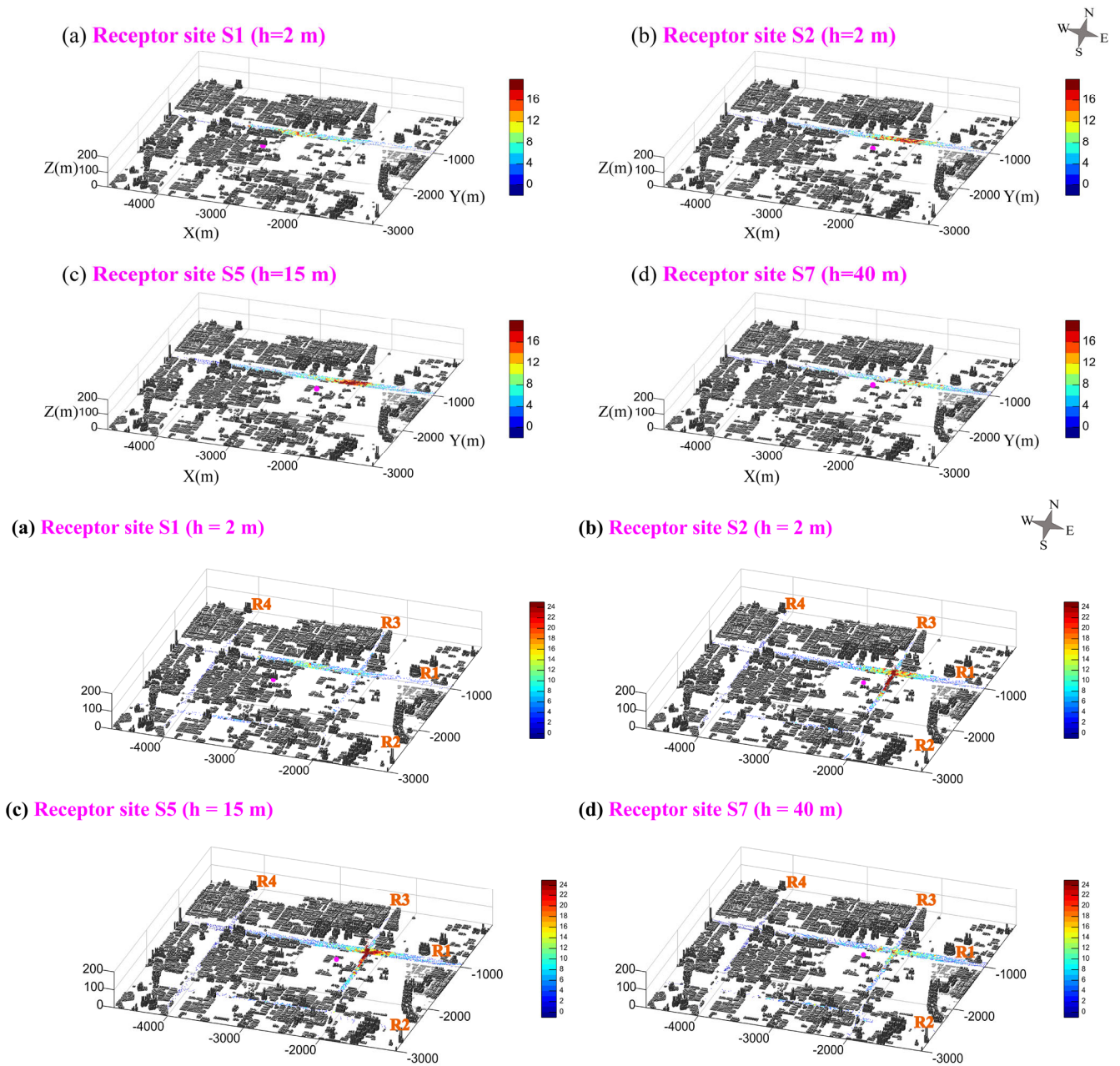


Figure 7: Density distribution (refers to the number of particles that have stayed in the space of $10\text{ m} \times 10\text{ m}$ in the horizontal direction and 5 m from the surface to above in the vertical direction) of all trajectory points passing through the traffic roads that ~~released~~received from different receptor sites (S1, S2, S5, and S7, see details in Table 43). The four receptor sites are all marked with magenta dots.

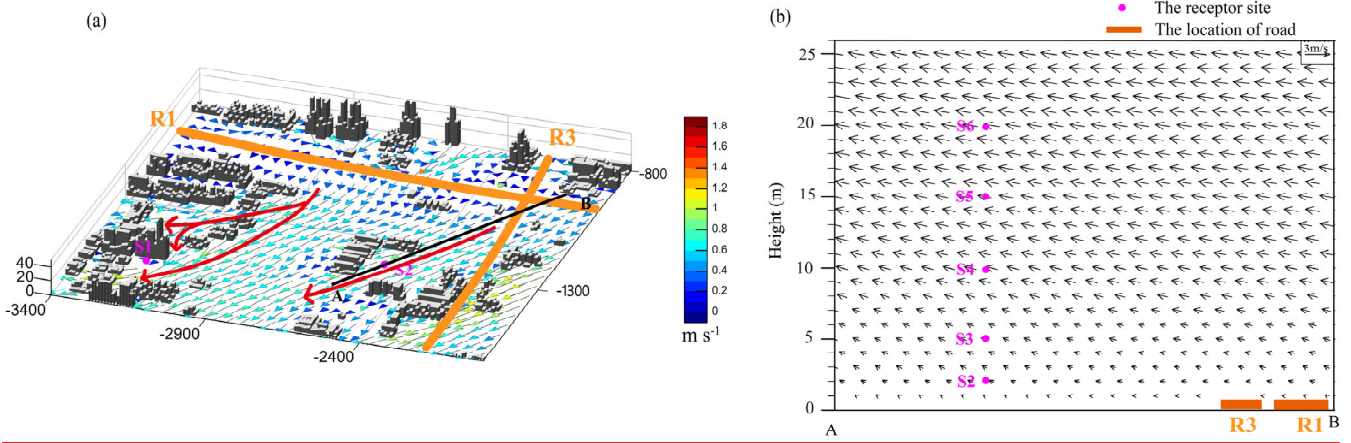


Figure 8: The (a) average surface wind and (b) vertical structure of average winds that along the wind direction around the receptor site S2 (line AB) in January 2019. The road R1 is marked with orange line; the location of the vertical profile is shown in black line, and the receptor sites S1 to S6 are all marked with magenta dots.

795

800

Table 1. The list of variables required to run FLEXPART and the sources of variables.

<u>variable</u>	<u>Description</u>	<u>Source</u>
<u>PB</u>	<u>base value of pressure</u>	<u>WRF</u>
<u>P</u>	<u>perturbation of pressure</u>	<u>WRF</u>
<u>PHB</u>	<u>base value of geopotential</u>	<u>WRF</u>
<u>PH</u>	<u>perturbation of geopotential</u>	<u>WRF</u>
<u>T</u>	<u>temperature</u>	<u>WRF</u>
<u>QVAPOR</u>	<u>specific humidity</u>	<u>WRF</u>
<u>MAPFAC_M</u>	<u>map factor</u>	<u>WRF</u>
<u>PSFC</u>	<u>surface pressure</u>	<u>STAR-CCM+</u>
<u>U10</u>	<u>10 m wind along x axis</u>	<u>STAR-CCM+</u>
<u>V10</u>	<u>10 m wind along y axis</u>	<u>STAR-CCM+</u>
<u>T2</u>	<u>2 m temperature</u>	<u>WRF</u>
<u>Q2</u>	<u>2 m dew point</u>	<u>WRF</u>
<u>SWDOWN</u>	<u>surface solar radiation (optional)</u>	<u>WRF</u>
<u>RAINNC</u>	<u>large scale precipitation (optional)</u>	<u>WRF</u>
<u>RAINC</u>	<u>convective precipitation (optional)</u>	<u>WRF</u>
<u>HFX</u>	<u>surface sensible heat flux (optional)</u>	<u>STAR-CCM+</u>
<u>U</u>	<u>wind along x axis</u>	<u>STAR-CCM+</u>
<u>V</u>	<u>wind along y axis</u>	<u>STAR-CCM+</u>
<u>W</u>	<u>Cartesian vertical velocity</u>	<u>STAR-CCM+</u>

Table 24 Parameterization scheme for the physical processes set up in the WRF model.

<u>Physical management</u>	<u>Parameterization</u>	<u>Reference</u>
Microphysics scheme	Lin	Lin et al. (1983)
Longwave radiation scheme	RRTMG	Iacono et al. (2008)
Shortwave radiation scheme	RRTMG	Iacono et al. (2008)
Land surface scheme	Noah	Chen and Dudhia (2001)
Planetary boundary layer scheme	MYNN3	Nakanishi and Niino (2006)

805

Table 32 Statistical performances of the hourly near-surface ~~meteorologies~~ meteorology simulated by the WRF model.

	<u>R</u>	<u>MB</u>	<u>ME</u>	<u>RMSE</u>
T	0.80	-1.86 (K)	2.33 (K)	2.82 (K)
RH	0.70	-5.95 (%)	11.5 (%)	15.0 (%)
P	0.98	3.66 (hpa)	3.66 (hpa)	3.77 (hpa)
WS	0.45	1.44 (m s ⁻¹)	1.58 (m s ⁻¹)	1.97 (m s ⁻¹)

810

Table R4. Locations of receptor sites and the corresponding potential contribution ratios.

<u>Receptor site</u>	<u>Location (x, y, z)</u>	<u>potential contribution ratio</u>				
		<u>R1</u>	<u>R2</u>	<u>R3</u>	<u>R4</u>	<u>All</u>
<u>S1</u>	<u>(-3200 m, -1420 m, 2 m)</u>	<u>1.81%</u>	<u>=</u>	<u>=</u>	<u>=</u>	<u>=</u>
<u>S2</u>	<u>(-2500 m, -1300 m, 2 m)</u>	<u>2.38%</u>	<u>0.18%</u>	<u>1.32%</u>	<u>0.16%</u>	<u>4.05%</u>
<u>S3</u>	<u>(-2500 m, -1300 m, 5 m)</u>	<u>2.57%</u>	<u>0.29%</u>	<u>1.28%</u>	<u>0.10%</u>	<u>4.25%</u>
<u>S4</u>	<u>(-2500 m, -1300 m, 10 m)</u>	<u>2.71%</u>	<u>0.32%</u>	<u>1.18%</u>	<u>0.12%</u>	<u>4.33%</u>
<u>S5</u>	<u>(-2500 m, -1300 m, 15 m)</u>	<u>2.98%</u>	<u>0.27%</u>	<u>1.22%</u>	<u>0.20%</u>	<u>4.67%</u>
<u>S6</u>	<u>(-2500 m, -1300 m, 20 m)</u>	<u>2.75%</u>	<u>0.37%</u>	<u>1.09%</u>	<u>0.17%</u>	<u>4.38%</u>
<u>S7</u>	<u>(-2500 m, -1300 m, 40 m)</u>	<u>2.30%</u>	<u>0.39%</u>	<u>0.70%</u>	<u>0.25%</u>	<u>3.64%</u>
<u>S8</u>	<u>(-2500 m, -1300 m, 50 m)</u>	<u>1.94%</u>	<u>0.57%</u>	<u>0.68%</u>	<u>0.36%</u>	<u>3.55%</u>

Table 3 Locations of receptor sites and potential contribution ratios of traffic sources.

<u>Receptor site</u>	<u>Location (x, y, z)</u>	<u>potential contribution ratio</u>
<u>S1</u>	<u>(-3200 m, -1420 m, 2 m)</u>	<u>1.81%</u>
<u>S2</u>	<u>(-2500 m, -1300 m, 2 m)</u>	<u>2.38%</u>
<u>S3</u>	<u>(-2500 m, -1300 m, 5 m)</u>	<u>2.57%</u>
<u>S4</u>	<u>(-2500 m, -1300 m, 10 m)</u>	<u>2.71%</u>
<u>S5</u>	<u>(-2500 m, -1300 m, 15 m)</u>	<u>2.98%</u>
<u>S6</u>	<u>(-2500 m, -1300 m, 20 m)</u>	<u>2.75%</u>
<u>S7</u>	<u>(-2500 m, -1300 m, 40 m)</u>	<u>2.30%</u>
<u>S8</u>	<u>(-2500 m, -1300 m, 50 m)</u>	<u>1.94%</u>